Mechanisms of Eastern Mediterranean Rainfall Variability

GIDON ESHEL

Department of the Geophysical Sciences, The University of Chicago, Chicago, Illinois

BRIAN F. FARRELL

Department of Earth and Planetary Sciences, Harvard University, Cambridge, Massachusetts

(Manuscript received 23 November 1998, in final form 20 January 2000)

ABSTRACT

This paper presents a simple theory for the association between observed eastern Mediterranean (EM) rainfall anomalies and North Atlantic (NA) climate variability. Large-scale NA atmospheric mass rearrangements, primarily a modulation of the Icelandic low and the subtropical high pressure systems, tend to extend beyond the NA. A particularly strong such teleconnection exists between the northern NA and southern Europe and the Mediterranean Basin. Pressure anomalies over Greenland–Iceland are thus associated with reversed-polarity anomalies centered over the northern Adriatic, affecting the entire Mediterranean Basin; elevated Greenland pressure is accompanied by an anomalous cyclone over the Mediterranean, and a Mediterranean high pressure system is present when pressure over Greenland is reduced. In the EM, these anomalies result in anomalous southerlies during Greenland highs, and northerlies during Greenland lows. Eastern Mediterranean southerlies warm the EM, while northerlies cool locally. Because heat advection by horizontal and vertical motions dominate the EM thermodynamic equation (or, put differently, because thickness advection dominates the omega equation), cooling by northerly winds results in enhanced subsidence. Conversely, warming by anomalous EM southerlies produces enhanced ascent. These vertical motion anomalies modify the stability of the mean column, resulting in the observed EM rainfall anomalies.

1. Introduction

In recent years, considerable attention has been devoted to climate variability outside the deep Tropics. Common to many of the mechanisms advanced by various authors to explain the variability are large-scale stationary wave anomalies (Battisti et al. 1995; Bladé 1997; Frankignoul 1985; Kushnir and Wallace 1989; Kushnir 1994; Latif and Barnett 1994, 1996; Molteni and Palmer 1993; Venzke et al. 1998; Wallace et al. 1990, 1992; Weng and Neelin 1998, among others). A discussion of stationary wave variability over the North Atlantic (NA) sector can be found in any of the above references. The basic structure of the variability is a fairly simple modulation of the relative intensity of the climatological subtropical high and subpolar low—the NA oscillation (NAO; e.g., Hurrell 1995; Kushnir 1994, 1999; McCartney 1997; Rodwell et al. 1999). This modification of the NA mean meridional pressure gradient and the associated thermal wind balance of the midlatitude westerlies affects the intensity and spatial details of the westerlies, and thus downstream climates. Especially relevant to the current study, Hurrell (1995) and Hurrell and van Loon (1997) have demonstrated the importance of the NAO to regional patterns of temperature and water vapor advection. Because anomalies associated with the NAO (and other extratropical stationary wave phenomena such as the Pacific–North America pattern) are typically centered over the ocean, they affect human populations primarily through their remote influences. These remote impacts have enjoyed less attention than the anomalies themselves, and their description and dynamical understanding are incomplete (Hurrell and van Loon 1997; Steinberger and Gazit-Yaari 1996). Here we explore a specific example of remote effects of stationary wave anomalies, namely, eastern Mediterranean (EM) climate anomalies associated with NA anomalies. While there is no reason to assume this example is physically unique, its societal impact is substantial. Dry summers (Rodwell and Hoskins 1996) render winter rainfall the sole, and highly capricious, source of renewable water in the EM. As most economies around the EM are still developing, they depend heavily on water, and are very susceptible to droughts. Thus both fundamental climatic processes

Corresponding author address: Dr. Gidon Eshel, Dept. of the Geophysical Sciences, The University of Chicago, 5734 S. Ellis Ave., Chicago, IL 60637.
E-mail: geshel@uchicago.edu

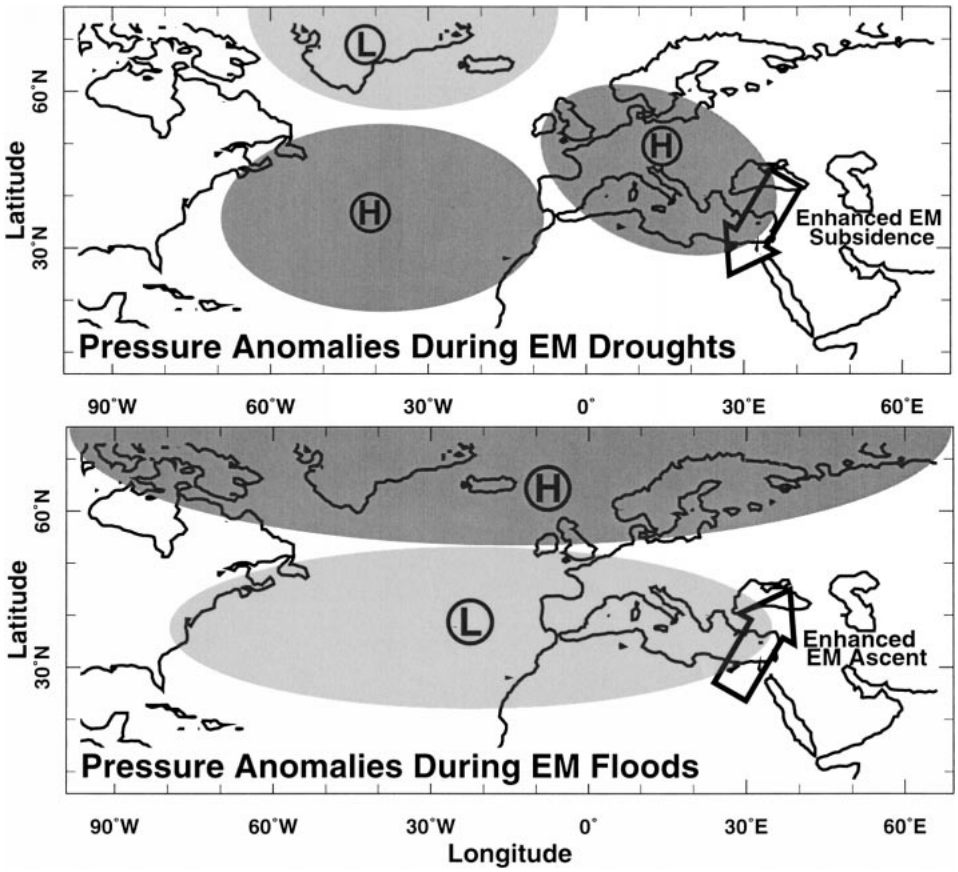

FIG. 1. Schematic of the NA–EM teleconnection. Eastern Mediterranean pressure anomalies are part of large-scale anomalies over the NA–Europe–Mediterranean sector. The Mediterranean experiences high (low) pressure anomalies during low (high) EM rainfall anomalies. This yields northeasterlies during times of low rainfall, and southwesterlies during high EM rainfall, shown by the thick arrows. During EM droughts, this anomalous wind cools the EM. The cooling is partly compensated by enhanced subsidence, which results in increased lower tropospheric static stability and suppressed precipitation. In times of high EM rainfall (lower panel), these processes are reversed.

and their socioeconomical consequences are manifested in the EM, and provide the motivation for this paper.

To enhance readability, we summarize in advance the main ideas of the paper here and in Fig. 1. We argue that EM rainfall variability is caused by subsidence anomalies associated with the NA. Variability of tropospheric mass distribution over the NA–Mediterranean sector assumes the form of a seasonally stationary wave pattern with opposite-sign nodes over Greenland–Iceland and the northern Mediterranean. Thus when Greenland's pressure is anomalously high, an anomalous low covers the Mediterranean and southern Europe, yielding EM southerlies; when Greenland pressure is anomalously low, EM northerlies prevail. These wind anomalies are strong and persistent, and significantly alter patterns of heat advection. The ensuing imbalance between the mass and motion fields is followed by dynamic adjustment. The adjustment process modifies subsidence intensity, strongly affecting rainfall. Enhanced subsidence and reduced EM rainfall accompany cooling by northerly winds characteristic of a Greenland low. Conversely, warming by southerly winds during Greenland highs results in weakened subsidence and intensified EM precipitation.

2. Data and analysis

For constructing spatial mean anomalies, we loosely define the EM as 32°–42°N, 22°–36°E, encompassing northern Israel, coastal Lebanon and Syria, and most of Turkey and Greece. In this region, there are 16 stations with sufficiently long measured rainfall records in the National Oceanic and Atmospheric Administration's (NOAA's) National Climatic Data Center Global Climate Perspectives System (GCPS) monthly station dataset (Baker et al. 1995), shown in Fig. 2. We augment this dataset with three stations in northern Israel (B. Rajagopalan, Lamont–Doherty Earth Observatory, Columbia University, 1998, personal communication) with similar temporal coverage. Combined, the stations are

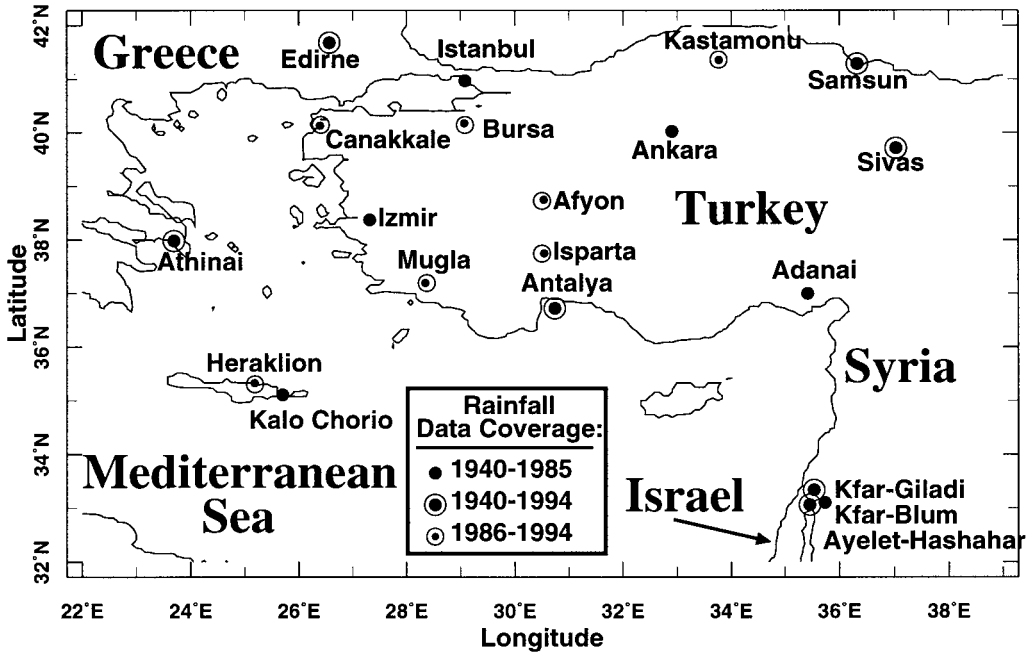

FIG. 2. Rain gauge station distribution, from the ungridded data of Baker et al. (1994). Symbols denote temporal coverage, as indicated by the legend.

distributed throughout the EM (thus sampling it reasonably well) and span a wide range of geographical settings and elevations. The resultant record is shown in Fig. 3b. It is discontinuous in 1985 as some station records end at that year and are replaced by records from nearby other stations, as indicated on Fig. 2. A good agreement between the records derived from the two station sets during 1980–85 (not shown) suggests that the effect of the change is minor.

The variability among the stations (given by the shading) is not negligible, as expected given the diverse geographies of the stations. However, the record as a whole follows the mean sufficiently tightly for some anomalies to clearly stand out above the variability. Differences in large-scale dynamical atmospheric state between periods of high and low EM rainfall anomalies are a central element of this paper. To choose the specific years to be studied, we employ the following considerations. First, since we wish to study large-scale dynamical states of the atmosphere, we do not consider anomalies before 1958, when the National Centers for Environmental Prediction (NCEP)–National Center for Atmospheric Research (NCAR) reanalysis data first become available (see below a discussion of the reanalysis). Before that time no consistent, complete record of the state of the atmosphere is available. In the post-1958 period, we choose the five driest and five rainiest years based on agreement between the station-derived record and the two gridded records shown in Fig. 3a. The fidelity of the gridded datasets is obviously of concern. Figure 2 of Hulme (1994, p. 392) shows the geographical locations of the stations the University of East Anglia (UEA) dataset comprises. For the relevant decades shown (1951–60 and 1981–90), the EM is well covered by reliable stations [as defined in Hulme (1994)]. Further, Hulme's Fig. 3 shows that in the $5° \times 5°$ version of the UEA analysis used in Fig. 3a, all EM grid points possess at least a 30-year time series (using the data treatment described by Hulme). Hence the UEA precipitation record appears robust and representative of the EM. Most extreme seasons of both signs are common to all datasets. The minor exception is 1987/88, which is the fifth rainiest year in the station and UEA's records, but is seventh in the NOAA GCPS record. The agreement among the gridded datasets shown in Fig. 3a, and among either one of them and the constructed one (Fig. 3b), further suggests that these datasets are collectively adequate for the purposes of the current study. We form canonical ''rainy'' and ''dry'' atmospheric states by averaging the October–March means of the five extreme seasons. Thus atmospheric states characterizing EM precipitation extremes represent averages of 5 winters $\times$ 6 months winter^{-1}. For brevity, we refer to the 30-month period of low EM precipitation as P_L, and to that of high EM precipitation as P_H.

Tropospheric variables (winds, humidity, temperature) are taken from the NCEP–NCAR reanalysis project (Kalnay et al. 1996). The reanalysis data are not ideally suited for our purpose, as they are not purely observed, but rather represent assimilation of observations into a state-of-the-art atmospheric GCM. While a blend of observed and modeled data is inferior to high quality, high (spatial and temporal) resolution observations, such a

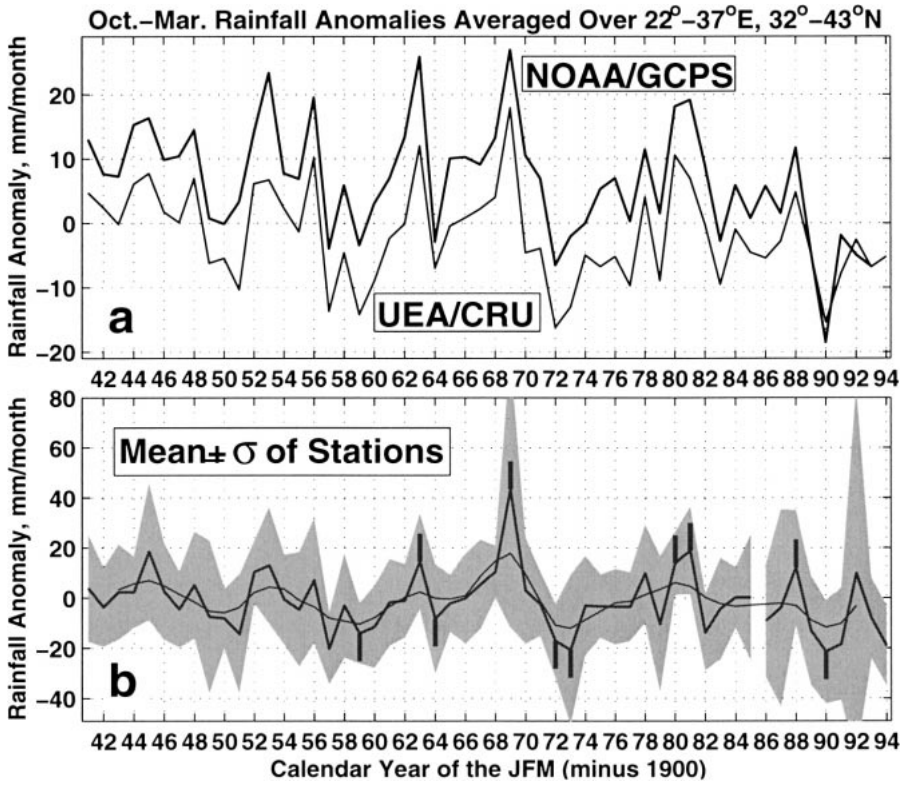

FIG. 3. Records of EM winter rainfall anomalies. (a) Two observational records of gridded precipitation anomalies; thick line, NOAA's NCDC GCPS (Baker et al. 1994); thin line, UEA/CRU (Hulme 1992, 1994). (b) Mean (thick solid line) and standard deviation (shaded region) of the station data shown in Fig. 1. The gap distinguishes the two data-coverage periods indicated on Fig. 1. The five rainiest and driest winters are denoted by small dashes originating from the corresponding data points up or down, respectively. The thin line is the mean (thick curve), convolved with [1, 2, 3, 2, 1]/9, i.e., a 5-yr weighted running mean.

dataset does not currently exist, and there is not enough station data to calculate dynamical fields (such as divergence) accurately. On the other hand, the model's thermodynamics are strongly constrained by data in data-dense regions such as the Mediterranean. For example, Trenberth and Guillemot (1998, their Fig. 3) present a global correlation map spanning 60 months of total-column precipitable water in the NCEP–NCAR reanalysis data versus remotely sensed observations [NASA Water Vapor Project (NVAP)]. Correlations exceed 0.90 throughout the NA, Mediterranean, and Europe, but drop somewhat to the south of the region of interest, toward the central Red Sea and the Sahara. Hence the dynamically consistent assimilated fields, while clearly imperfect, are the best currently available approximation to the true fields. Transient errors are averaged out in the monthly mean data we use, and are further reduced by the 30-month averaging described above. Similarly, the characteristic space scales for the anomalies analyzed here are fairly large [typically $O(10 \times 10$ grid points)], and are thus relatively immune to small-scale noise in the assimilation model. Our results should therefore be considered tentative, awaiting future improvements of the observational network. With the exception of rainfall and surface wind stress [calculated from ship wind estimates (daSilva et al. 1994)], data are from the reanalysis project.

Significance tests

We present significance levels of both anomalies a and correlations r, employing the t test. To form t statistics, we use $t = r[(df - 2)/(1 - r^2)]^{1/2}$ and $t = (a - \overline{a})/\sigma_a^t$ (Philips 1982), where $\overline{a}$ and σ_a^t are a's temporal mean and standard error. In estimating the number of degrees of freedom df, we make the rather stringent assumption that the decorrelation timescale ~2 yr (i.e., that only every 2-yr period represents an independent realization; df = $N/2$, where N is the time series length in years). [Typical gridpoint autocorrelation functions of used anomaly fields indicate that actual characteristic temporal decorrelation scales are typically less (often much less) than 10 months on average. Hence, the assumption of a 2-yr decorrelation timescale represents a conservative upper bound.] To exclude spurious correlations primarily due to trends in the data, all reported

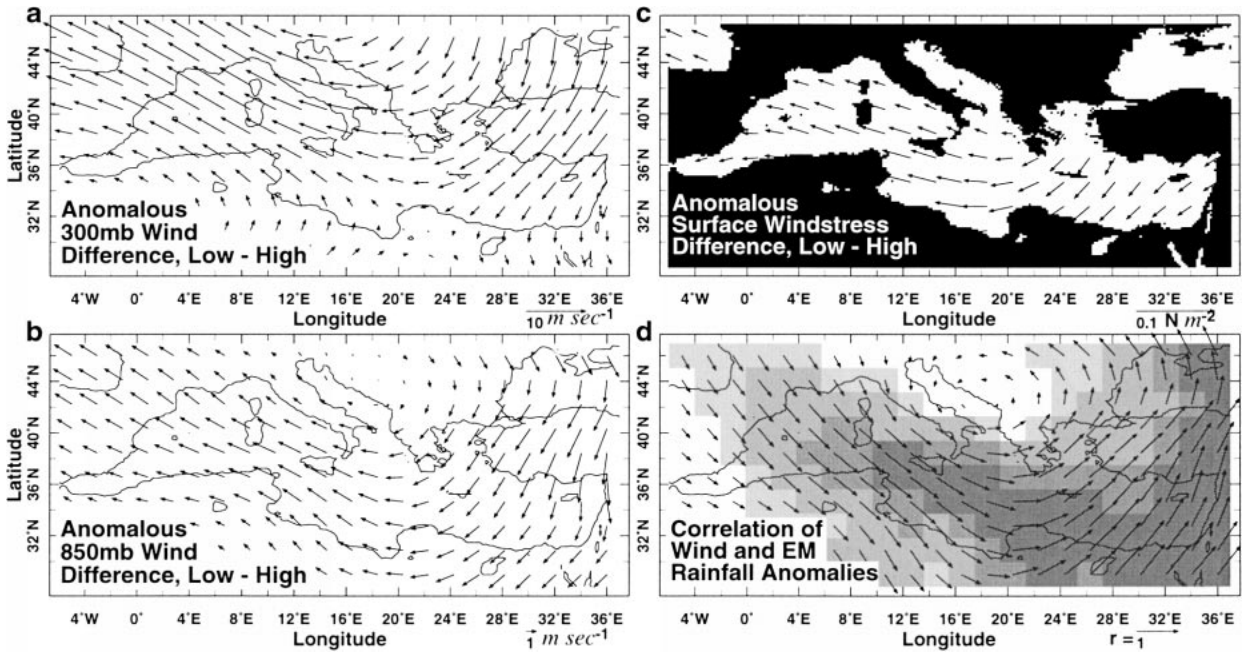

FIG. 4. (a), (b) Wind anomaly differences in m s^{-1} (scale arrows shown in the lower-right corner of each panel) between extreme EM rainfall anomalies at 300 and 850 mb (Kalnay et al. 1996). (c) Estimated surface windstress anomaly difference in N m^{-2} from ship wind reports (daSilva et al. 1994). (d) Local correlations of anomalous 850-mb winds and seasonal EM rainfall anomalies. Light to dark shadings indicate *t*-test significance of the correlation magnitudes of 0.1, 0.05, 0.01, and 0.005, as described in the text.

correlations are computed after linear trends present in the various records have been removed by a least squares best fit procedure. The calculated t values are compared with critical ones (t_c) obtained from the t distribution with df. When $|t| > t_c$, the value (either anomaly or correlation) is assumed locally significant.

3. Large-scale anomalies during EM rainfall extremes

Figures 4a,b show the difference in wind anomalies between P_L and P_H in the upper and lower troposphere (i.e., the panels represent differences of means, each taken over five 6-month seasons, so that each panel is based on 60 monthly mean anomalies). Wind anomalies during P_L (P_H) comprise a Mediterranean-wide anticyclone (cyclone) centered north of the Adriatic (Fig. 4, with stronger P_L anomalies, as we found to be the case for all considered anomalies). The low-level anomalies are intense enough to effect the total fields. That is, there are total-field EM southwesterlies during P_H, and northerlies to northwesterlies during P_L; since climatological winds are much stronger at 300 mb, the anomalies have an essentially undetectable effect on the total field there. Consequently, and since our primary interest here is precipitation, which originates mainly from the lower- to midtroposphere (water vapor perturbations discussed later are orders of magnitude smaller in the upper troposphere), we concentrate on 850 mb. The vertical structure of the anomalies revealed by Fig. 4 is roughly equivalent barotropic during both P_L and P_H, which suggests that 850 mb adequately represents tropospheric processes. The fact that the water vapor forcing is most robustly manifested in the lower troposphere does not imply that EM precipitation variability is dynamically driven by lower-tropospheric processes. Rather, it is a simple consequence of the rapid decrease of water vapor mixing ratio with height. In fact, the advective thermal processes we describe below (and attribute the EM rainfall variability to) occur throughout the depth of the troposphere, as can be expected from the proposed teleconnective nature and Fig. 4. We revisit the height dependence of the anomalies later.

In addition to revealing the vertical structure of the anomalies, Fig. 4c (which is derived from a different dataset than Figs. 4a,b,d) is also an independent check on the reanalysis anomalies. Figure 4d shows that EM rainfall anomalies are strongly and significantly related to 850-mb wind anomalies not only during extreme droughts and floods (a and b) but also during more moderate conditions. High precipitation is associated with EM southwesterlies, while EM droughts accompany northerly and northeasterly local winds. The anomalous flows appear counterintuitive at first; during enhanced precipitation (P_H), the EM is downstream of the Sahara, while during P_L it is downstream of the relatively cold and rainy southeast Europe. This suggests that simple low-level moisture convergence is *not* the

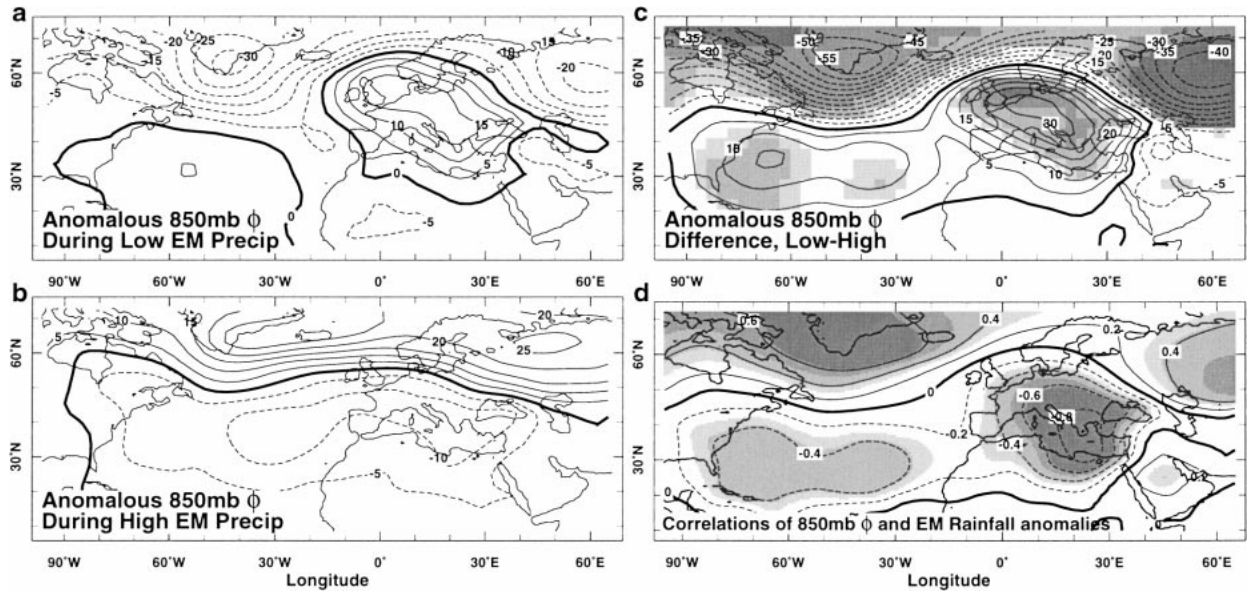

FIG. 5. EM geopotential height anomalies at 850 mb (Kalnay et al. 1996), in dynamic meters. (a), (b) Anomalies during extreme EM rainfall anomalies. (c) The height anomaly difference between the two extremes. (d) A correlation map over 37 yr of height anomalies with EM rainfall anomalies (Fig. 3). Both fields are linearly best fit detrended prior to computing correlations. The four shading levels represent *t*-test significance [of the anomaly differences in (c) and the correlations in (d)] of 0.1, 0.05, 0.01, and 0.005, as described in the text. Contour interval is 5 m in (a), (b), and (c), and 0.2 in (d).

primary cause of the precipitation anomalies, as might be reasonably expected (and as is quantified below).

Figure 5 shows the 850-mb height anomalies $\langle \tilde{\phi}_{850} \rangle$ with which the Mediterranean wind anomalies (Fig. 4) are consistent (where $\tilde{\cdot}$ denotes monthly mean deviation from monthly mean climatology, and $\langle \cdot \rangle$ denotes averaging over the 30 months of the five extreme seasons). This figure places the Mediterranean wind anomalies in a broader context, showing that P_L and P_H represent opposite extremes of a hemisphere-scale oscillation. Over the NA, very clear $\langle \tilde{\phi}_{850} \rangle$ nodes emerge, roughly coinciding with those of the full field (the Icelandic low and Subtropical high). In fact, despite being constructed based on EM (and not NA) variability, the resulting patterns are somewhat similar to the NAO pattern (Hurrell 1995), especially during high EM rain (Fig. 5b). {However, the spatial pattern related to EM droughts (Fig. 5a) is rather different from the NAO's [e.g., Hurrell's (1995) Fig. 1b]}. In any case, the high-amplitude, large-scale patterns (Figs. 5a,b,c) suggest that EM rainfall strongly covaries with NA variability. In both P_L and P_H the Mediterranean anomalies are opposite in sign to those over the northern NA, and similar in sign to those over the subtropical NA.

To go beyond the extreme conditions and the limited temporal coverage of P_L and P_H, Fig. 5d presents the correlation map of winter $\tilde{\phi}_{850}(x, y,$ yr) and the time series of seasonal EM rainfall anomalies (Fig. 3). The four shading levels represent *t* tests of correlation significance of 0.1, 0.05, 0.01, and 0.005, where we assume again the number of degrees of freedom df is half the number of time points. In Fig. 5d, correlations throughout most of the subpolar and subtropical gyres are significant at levels <0.05, and achieve significance <0.005 over most of the subpolar gyre. While not proving causality, the highly significant correlations show that the NA–EM relationship during extreme conditions (Figs. 5a,b,c) holds also during moderate anomalies, and strongly suggest that EM precipitation anomalies are dynamically linked to the NA.

a. Thermal anomalies due to horizontal motions

The wind anomalies (Fig. 4) induce high-amplitude, spatially coherent temperature tendency anomalies. While the interconnected physics of heat advection and EM rainfall are discussed in later sections, their relation is suggested a priori by their strong cross correlations throughout the Mediterranean (not shown), with significance of 0.05–0.005 over most of this region.

To facilitate the analysis using monthly mean fields, let us introduce the somewhat unusual decomposition $f \equiv f_c + \tilde{f} + f'$, where f is a generic field whose monthly climatology is f_c, $\tilde{f}$ is the monthly mean deviation from f_c, and f' is the instantaneous deviation from $\tilde{f}$ [i.e., with $\tilde{\cdot}$ denoting monthly averaging, $\tilde{\tilde{f}} = \tilde{f}$, and $(\tilde{f})_c = \overline{\tilde{f}'} = 0$ by construction]. With flow and temperature thus decomposed (and ∇ denoting the 2D gradient on pressure surfaces), the monthly mean heat advection is

$$\overline{\mathbf{V} \cdot \nabla \theta} = \mathbf{V}_c \cdot \nabla \theta_c + \mathbf{V}_c \cdot \nabla \tilde{\theta} + \tilde{\mathbf{V}} \cdot \nabla \theta_c + \tilde{\mathbf{V}} \cdot \nabla \tilde{\theta} + \overline{\mathbf{V}' \cdot \nabla \theta'},$$

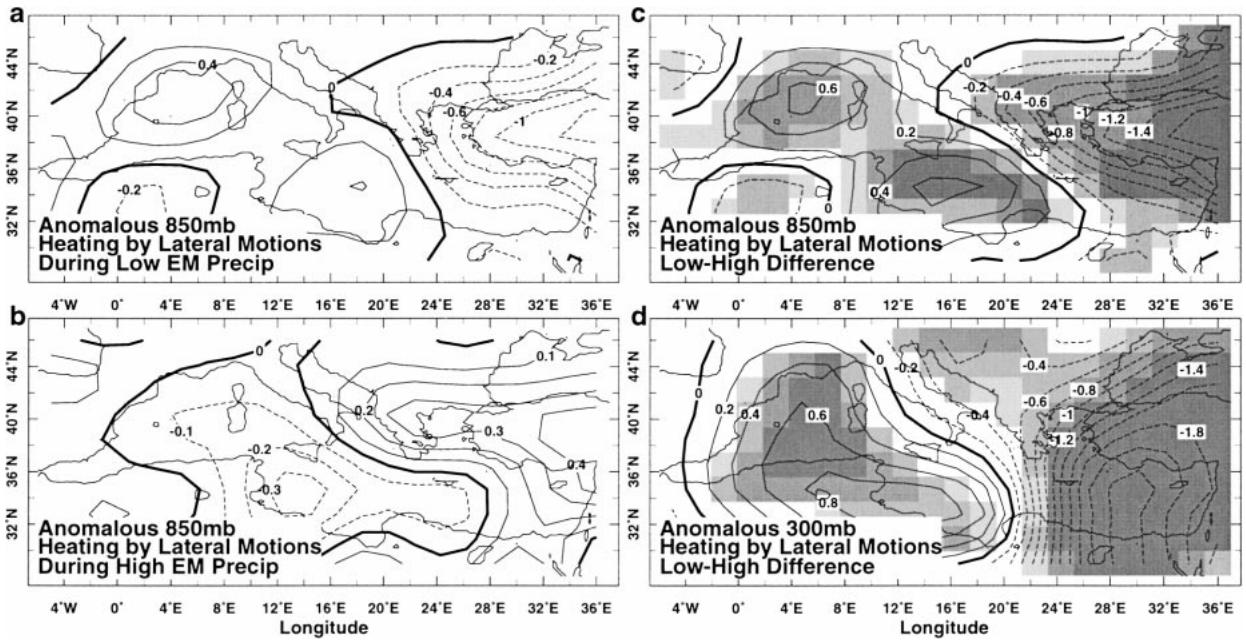

FIG. 6. Average anomalies during the five extreme EM rainfall seasons (30 months combined) of horizontal heat advection by monthly mean anomalies at 850 and 300 mb, in K day^{-1} (Kalnay et al. 1996). The shown anomalies comprise terms I–III of Eq. (1). Shading levels indicate *t*-test significance as described in the caption of Fig. 4 and in the text. Contour interval is 0.2 K day^{-1} in (a), (c), and (d), and 0.1 K day^{-1} in (b).

whose monthly mean anomaly (deviation from monthly climatology) is

$$\overline{\mathbf{V}\cdot\boldsymbol{\nabla}\theta}-(\overline{\mathbf{V}\cdot\boldsymbol{\nabla}\theta})_c=\overbrace{\mathbf{V}_c\cdot\boldsymbol{\nabla}\tilde{\theta}}^{\text{I}}+\overbrace{\tilde{\mathbf{V}}\cdot\boldsymbol{\nabla}\theta_c}^{\text{II}}+\overbrace{[\tilde{\mathbf{V}}\cdot\boldsymbol{\nabla}\tilde{\theta}-(\tilde{\mathbf{V}}\cdot\boldsymbol{\nabla}\tilde{\theta})_c]}^{\text{III}}+\overbrace{[\overline{\mathbf{V}'\cdot\boldsymbol{\nabla}\theta'}-(\overline{\mathbf{V}'\cdot\boldsymbol{\nabla}\theta'})_c]}^{\text{IV}}. \quad (1)$$

Here $\mathbf{V}$ is wind vector and θ is potential temperature. Averages of terms I–III of Eq. (1) at 850 mb during P_L and P_H (times -1, for temperature tendencies) are shown in Figs. 6a,b, while the $P_L - P_H$ difference, highly significant over most of the Mediterranean, is shown in Fig. 6c. The panels show that anomalous heat advection induces high-amplitude, spatially coherent thermal tendencies over most of the Mediterranean, with EM cooling during P_L and warming during P_H. Figure 6d shows that the advectively induced thermal anomalies are similar throughout the troposphere, consistent with Fig. 4. Since even at 850 mb the thermal anomalies shown in Fig. 6 are much larger than the ones due to anomalous latent heating by the rainfall anomalies (and are of the same sign), other processes must be actively restoring balance; below we argue that vertical motion anomalies are the key process.

The term dominating anomalous heat advection is the interaction of monthly mean wind anomaly (mostly north–south, as Fig. 4 shows) and climatological temperature gradient (not shown, also nearly meridional), that is, term II in Eq. (1). Interaction of the climatological westerly wind and anomalous temperature gradient [term I in Eq. (1)] is small. For example, during P_L the upstream western Mediterranean is warmer than climatology while the EM is colder, yet the EM temperature tendency due to horizontal heat advection is negative, -1.4 K day^{-1} (throughout the paper, ''horizontal'' refers to the pressure, rather than height, vertical coordinate). The reverse is true during P_H, and in general $\tilde{\mathbf{V}}\cdot\boldsymbol{\nabla}\theta_c \gg \mathbf{V}_c\cdot\boldsymbol{\nabla}\tilde{\theta}$ over the EM. Because anomalous temperature gradients are often nearly normal to flow anomalies (i.e., the flow anomalies are nearly barotropic and geostrophic), $\tilde{\mathbf{V}}\cdot\boldsymbol{\nabla}\tilde{\theta}\simeq(\tilde{\mathbf{V}}\cdot\boldsymbol{\nabla}\tilde{\theta})_c \simeq 0$, rendering term III of Eq. (1) generally unimportant.

The remaining Reynolds term [term IV of Eq. (1)] represents the role of submonthly wind–temperature correlations in the total heat balance. Figure 7 shows the temperature tendency due to horizontal anomalous eddy heat advection (defined by submonthly timescales; the vertical component, $-\langle\overline{\omega'\partial_p\theta'}-(\overline{\omega'\partial_p\theta'})_c\rangle$ is negligible, and is not shown). While spatially and temporally coherent, with highly significant $P_L - P_H$ differ-

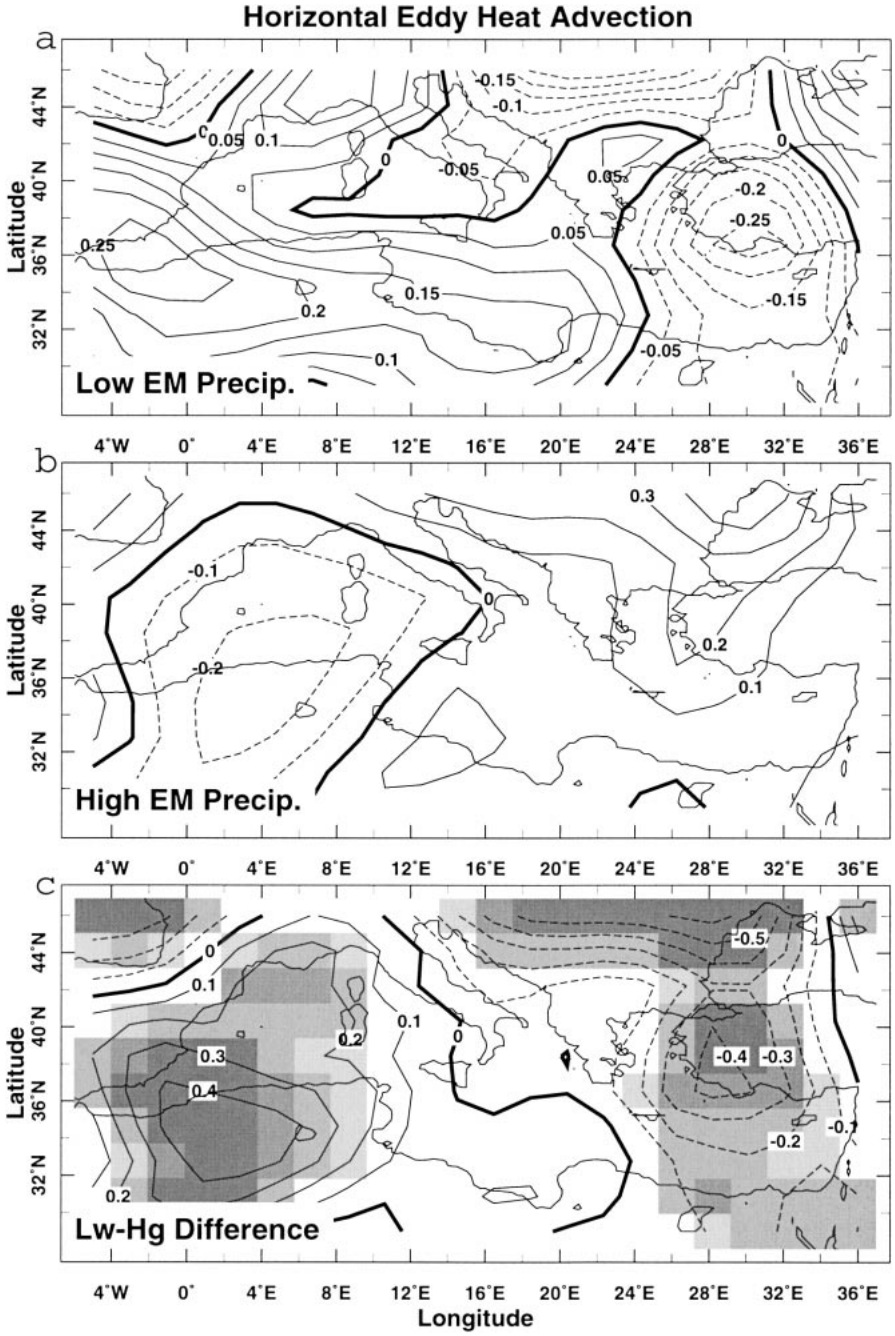

FIG. 7. Average anomalies during the five extreme EM rainfall seasons (30 months combined) of horizontal heat advection by eddy anomalies at 850 mb, in K day^{-1} (Kalnay et al. 1996). The shown anomalies represent term IV of Eq. (1). Shading levels indicate *t*-test significance as described in the caption of Fig. 4 and in the text. Contour interval is 0.05 K day^{-1} in (a), and 0.1 K day^{-1} in (b) and (c).

ences (Fig. 7c), the eddy heat advection is smaller than the corresponding advection by monthly mean anomalies (Fig. 6). More important, the sense of the anomalous eddy heat advection is to further upset—rather than restore—the thermal balance due to heat advection by monthly mean anomalies. By increasing anomalous temperature tendencies due to heat advection in both P_L and P_H, anomalous eddy heat advection increases thermal disequilibrium; term IV of Eq. (1) is *not* the one responsible for balancing the heat budget. However, this

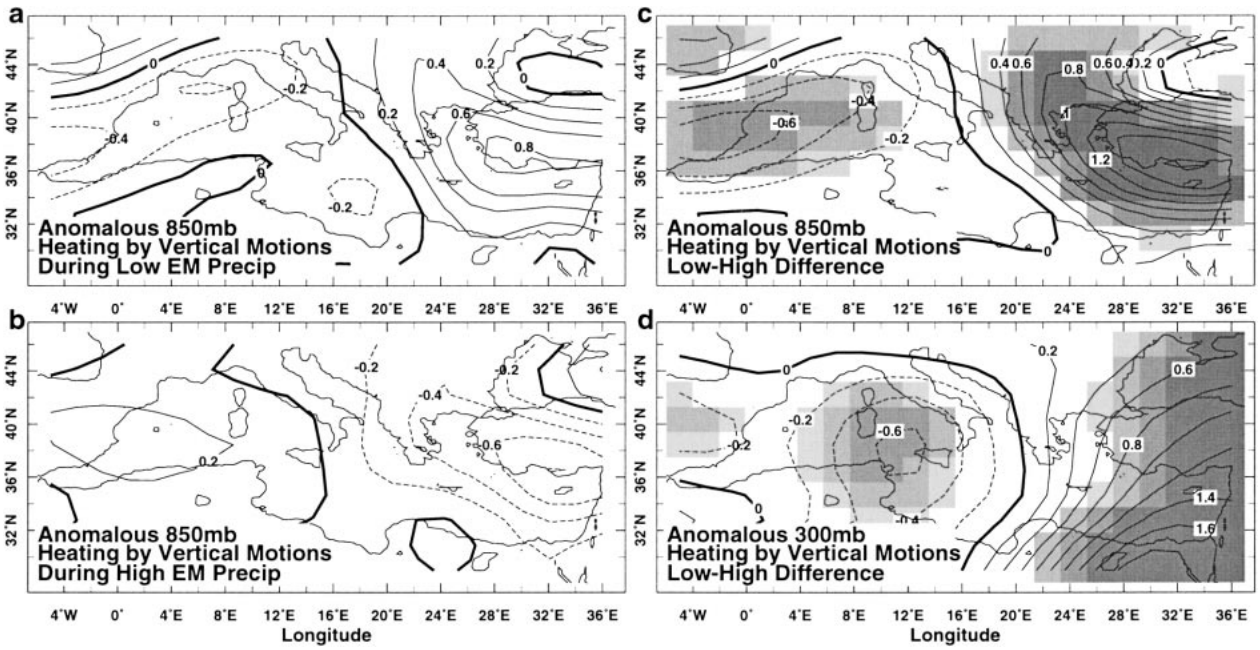

FIG. 8. Average anomalies during the five extreme EM rainfall seasons (30 months combined) of vertical heat advection by monthly mean anomalies at 850 and 300 mb, in K day^{-1} (Kalnay et al. 1996). This is the vertical analog of Fig. 6. Contour interval is 0.2 K day^{-1} in (a)–(d).

does not indicate a negligible role for anomalous eddy activity, as discussed below.

Thus advection anomalies by eddies, at least narrowly defined by submonthly timescales, are of the wrong sign to restore balanced budgets. This seems to disagree with the prevalent ideas about NAO driven variability (Hurrell 1995; Hurrell and van Loon 1997), which emphasize storm track variability; because synoptic timescales are <1 month, it is reasonable to expect term IV of Eq. (1) to represent the greater part of this effect. However, this need not be the case. When storm activity is persistent and recurrent enough, as is often observed, the storms are able to alter monthly means. Then, the storms' effects are absorbed by monthly mean terms in Eq. (1) (terms I–III), reconciling Hurrell's emphasis on storm track variability with the relative smallness of Eq. (1)'s term IV.

This section can thus be summarized by approximating the source of anomalous heat advection in Eq. (1) as

$$\overline{\mathbf{V}\cdot\boldsymbol{\nabla}\theta} - (\overline{\mathbf{V}\cdot\boldsymbol{\nabla}\theta})_c \simeq \tilde{\mathbf{V}}\cdot\boldsymbol{\nabla}\theta_c, \qquad (2)$$

that is, as the interactions of monthly mean wind anomalies with the climatological temperature gradient, where the approximation has been obtained empirically, not formally through scale analysis or expansion in a small parameter. Equation (2) thus explains the antisymmetry of Fig. 6's panels as the consequence of essentially zonal climatological temperature distribution and the wind patterns shown in Fig. 4, where wind anomalies in the EM are opposite to those in the western Mediterranean.

b. Thermal anomalies due to vertical motions

The thermal anomalies discussed in the previous section are very large; eddies and monthly mean horizontal motions combine to yield an EM cooling of up to 1.5 K day^{-1} during P_L, and a warming of $\sim$0.5 K day^{-1} during P_H. Clearly, such anomalous tendencies are not sustainable, and must be balanced by other processes. The key process counteracting the thermal anomalies due to horizontal motions and eddies is the other leading term in the thermodynamic equation, heating by vertical motions. Figure 8 shows the monthly mean anomalous subsidence heating. While Fig. 8 presents the total vertical heat advection, the interaction of the anomalous flow and the climatological θ gradient ($-\tilde{\omega}\partial_p\theta_c$) is the only major contributor, as in the horizontal advection case. A comparison of Figs. 6 and 8 reveals that spatial patterns of horizontal and vertical heat advection are similar [with the clear antisymmetry due to the wind anomalies (Fig. 4) in both], and oppose each other. The partial cancellation is of course imperfect, emphasizing the collective importance of other processes such as diabatic heating anomalies, advection by anomalous eddies, etc.

To strengthen the case for the proposed connection between EM subsidence and horizontal wind anomalies (through their advective thermal effects), Fig. 9 presents

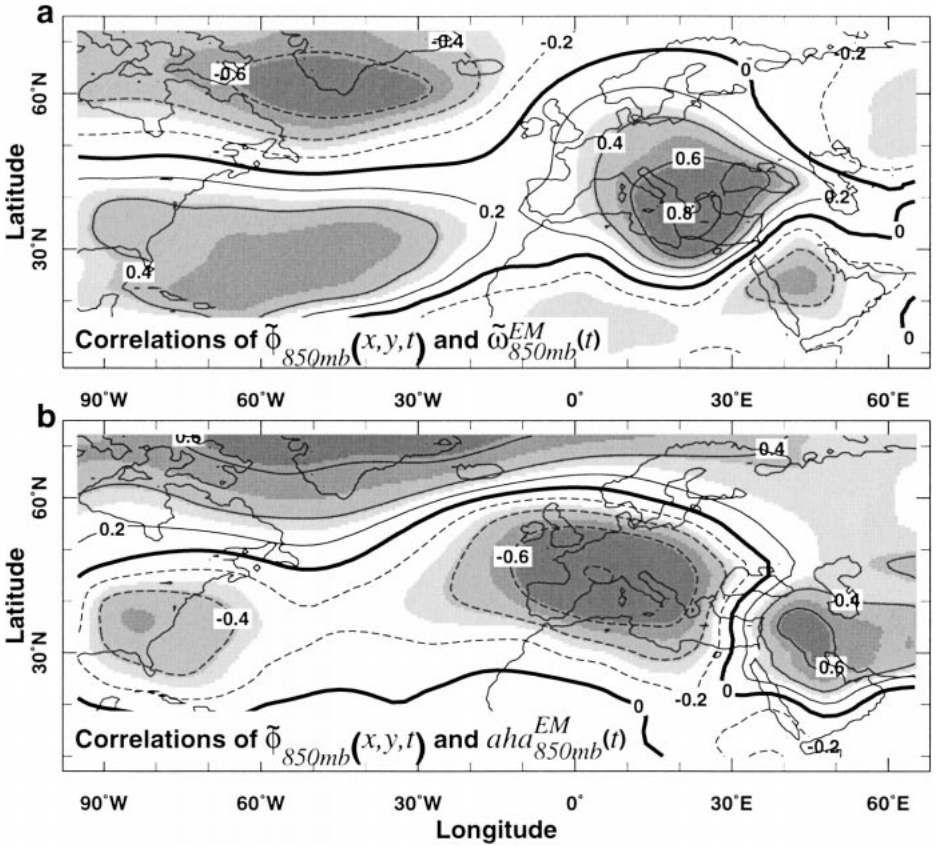

FIG. 9. Correlation maps of 850-mb geopotential height anomalies with time series of (a) anomalous subsidence and (b) heat advection (aha), spatially averaged over the EM (Kalnay et al. 1996). The four shading levels represent *t*-test significance of 0.1, 0.05, and 0.01, and 0.005, assuming a decorrelation timescale of ~2 yr, as described in the text. Correlated fields are first linearly best fit detrended in time. Contour interval is 0.2 in (a) and (b).

correlations of $\tilde{\phi}_{850}(x, y, \text{yr})$ (the scalar field best representing vector winds) with two 850-mb variables, spatially averaged over the EM. In Fig. 9a, $\tilde{\phi}_{850}$ is correlated with EM mean subsidence, $\tilde{\omega}_{850}(\text{yr})$ (with shading indicating significance levels of 0.1, 0.05, 0.01, and 0.005, using the previously described procedure). As in Fig. 5d, strong and spatially coherent correlations with the subtropical and subpolar gyres are apparent, and are significant at <0.05 levels. An area 40° longitude $\times$ 10° latitude near southern Greenland is significant at <0.005. Figure 9a suggests not only that EM subsidence strongly covaries with local winds (at least with their geostrophic part) but also that those latter anomalous winds are intimately related to the NA. Like the correlations of Fig. 5d, Fig. 9 is thus consistent with the proposed physical mechanism. In Fig. 9b, $\tilde{\phi}_{850}$ is correlated with EM mean anomalous heat advection (aha). While the details are different from Fig. 9a and Fig. 5d, the three principal nodes are reproduced, albeit somewhat altered and spatially shifted. These differences, expected given the noise levels in all participating variables, do not mask the basic message: anomalies of EM subsidence and heat advection individually covary with essentially the same Mediterranean and NA geopotential height anomalies. Figure 9 thus lends observational support to the proposed physical mechanism linking EM subsidence and heat advection to each other, and to the NA.

c. The approximate thermal balance

Of primary importance to EM rainfall is the approximate balance of the two leading terms in the anomalous heat budget,

$$-\tilde{\mathbf{V}} \cdot \nabla \theta_c \simeq \tilde{\omega} \partial_p \theta_c. \tag{3}$$

The central importance to EM climate of essentially the same relation (with the additional diabatic term) has been emphasized by Rodwell and Hoskins (1996) in their elegant theory of EM summer aridity [their Eq. (3)]. It is striking that their insights, gained while addressing a very different situation (the upper troposphere, summer, and climatological conditions), apply so readily also to lower-troposphere winter anomalies.

Equation (3) suggests that the subsidence anomalies (essentially Fig. 8 rescaled) and the horizontal advective thermal anomalies are dynamically mutually consistent, satisfying

$$\tilde{\omega} \simeq -(\tilde{\mathbf{V}} \cdot \boldsymbol{\nabla}\theta_c)(\partial_p \theta_c)^{-1}. \tag{4}$$

The validity of Eqs. (3) and (4) is corroborated by the fact that individual gridpoint correlations between $\tilde{\omega}$ and $(\mathbf{V} \cdot \boldsymbol{\nabla}\theta) - (\mathbf{V} \cdot \boldsymbol{\nabla}\theta)_c$ are between -0.5 and -0.7 (significant at <0.05) over most of the Mediterranean. Further, the correlations reach significance <0.01 over a sizable area covering northwest Italy, southeast France, and the Gulf of Lions. Most important, the correlations over the entire EM reach values <-0.8 (significance < 0.005).

Combined, the anomalous horizontal winds (Fig. 4), their thermal consequences (Figs. 6 and 8), and the vertical motions implied by Eq. (4) provide a concise description of the mechanism underlying the EM precipitation anomalies. Climate anomalies in the NA are associated with stationary wave perturbations over the NA–Europe–Mediterranean sector. Operating primarily on the (weakly varying) climatological thermal gradients, wind anomalies accompanying the wave perturbations modify patterns of thermal advection. While other terms (e.g., diabatic heating) are not negligible, thermal advection by anomalous horizontal and vertical winds dominate and approximately cancel throughout the troposphere (Figs. 6 and 8). That is, the motions are approximately thermally neutral (isentrope following). Finally, the resultant subsidence anomalies give rise to the observed rainfall anomalies, as described below. This interpretation, and Eqs. (2) and (4), predict horizontal advective cooling and enhanced subsidence during northerly wind anomalies, and horizontal advective warming and reduced subsidence for southerly wind anomalies. This expectation is clearly borne out by the data, as a comparison of the east–west antisymmetries of Figs. 4, 6, and 8 immediately reveals.

d. Other processes potentially affecting subsidence anomalies

While in previous sections subsidence anomalies are diagnosed in terms of perturbations to the thermodynamic equation, other processes can induce ω anomalies, as the omega equation demonstrates. Simplified for illustrative purposes, the ω equation [e.g., Holton 1992, Eq. (6.29)] can be qualitatively recast as

$$\omega \sim -\frac{\partial}{\partial p}(\mathbf{V}_g \cdot \boldsymbol{\nabla}\xi) - \mathbf{V}_g \cdot \boldsymbol{\nabla}\frac{\partial \Phi}{\partial p}, \tag{5}$$

where ξ is the vertical component of the quasigeostrophic (QG) absolute vorticity, Φ is the geopotential, and the remaining notation is standard, and follows Holton (1992). Equation (5)'s second rhs term represents thickness advection that is proportional to thermal advection discussed above. The first rhs term, height-dependent absolute vorticity advection, is not addressed above yet is potentially important. We have therefore evaluated both of these ω-inducing processes in the EM. The earlier results based on the thermodynamic equation are closely reproduced by the QG analysis (the magnitude and spatial patterns of $\mathbf{V}_g \cdot \boldsymbol{\nabla}\partial_p\Phi$ strongly resemble Fig. 6). However, ω induction by height-dependent absolute vorticity advection proves spatially and temporally incoherent, and often (but not always) smaller then the thermal contribution. This result indicates that while differential vorticity advection can be locally and occasionally important, it is not as useful for analyzing low-frequency subsidence variability as anomalous heat advection. This conclusion is consistent with the approximate equivalent barotropic structure of the anomalies mentioned earlier.

e. The anomalous moisture budget

Unlike the thermodynamic equation, in which the source term is generally small, the water vapor equation contains a leading-order source term, the rainfall anomalies themselves. Three processes balance these water vapor anomalies. Horizontal moisture advection by monthly mean anomalies (not shown; mostly $\tilde{\mathbf{V}} \cdot \boldsymbol{\nabla}q_c$ where q is specific humidity) tends to have small spatial scales, and is generally relatively small. It tends to dry the EM during P_L and moisten it during P_H, partially counteracting the rain anomalies. While also secondary, moisture advection by eddies can be occasionally locally important (e.g., over Turkey during P_L, where they moisten at <0.12 g kg^{-1} day^{-1}). However, the leading term balancing EM moisture perturbations is anomalous vertical moisture advection due to monthly mean anomalies, shown in Fig. 10. As in the thermal equation, while Fig. 10 shows the full anomaly, it is dominated by the interactions of the anomalous flow with the climatological moisture gradient, $\tilde{\omega}\partial_p q_c$. Thus the approximate water vapor conservation can be written as

$$P \simeq -\int_0^h \frac{\rho_a}{\rho_w}\tilde{\omega}\frac{\partial q_c}{\partial p}\, dz, \tag{6}$$

where P is the precipitation rate in m day^{-1}, h is the thickness of the precipitating layer, and ρ_a and ρ_w denote air and water densities. The rhs of Eq. (6) is the net imbalance between the water vapor mass advected into and out of the precipitating layer. Because q values are very small in the upper troposphere, even if condensation occurs there it contributes very little to the total-column precipitation (note the order of magnitude drop between Figs. 10c and 10d). Consequently, the rhs integral can be truncated at a reasonable height above which condensation yields insignificant liquid water mass; for the EM $h \simeq 4$ km is roughly appropriate (which is the reason we concentrate mostly on the lower troposphere in our analyses). Taking a characteristic ver-

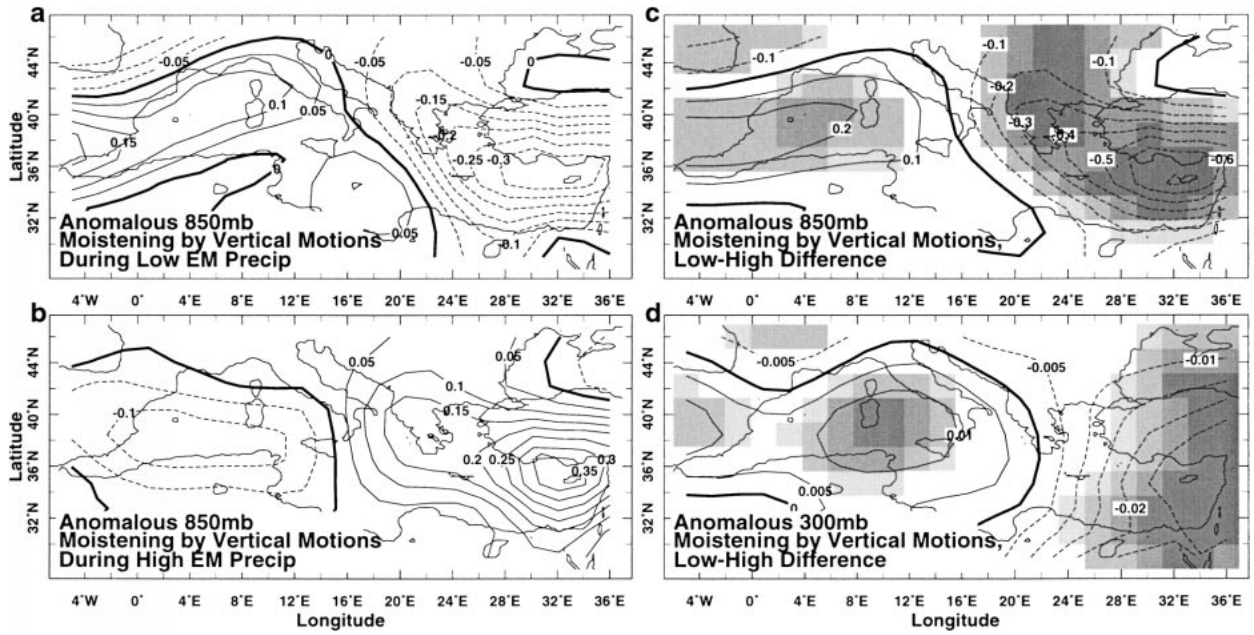

FIG. 10. Mean anomalies of moisture advection by monthly mean anomalies at 850 and 300 mb during extreme EM rainfall anomalies, in g kg^{-1} day^{-1} (Kalnay et al. 1996). This figure is analogous to Fig. 8, with specific humidity replacing heat. As before, shading levels indicate significance. Contour interval is 0.05 g kg^{-1} day^{-1} in (a) and (b), 0.1 in (c), and 0.005 in (d).

tical and spatial mean EM moisture tendency related to advection by monthly means of 0.3 g kg^{-1} day^{-1}, $\rho_a \simeq$ 0.7 kg m^{-3}, and $h \sim 4$ km yields $P \simeq 25$ mm month^{-1}, in order of magnitude agreement with Fig. 3. Thus while the heat balance represents approximate cancellation between horizontal and vertical advection, the leading moisture balance is between vertical advection and precipitation, with eddies and horizontal advection locally important.

4. Discussion and main conclusions

Our interpretation of the data is as follows. Eastern Mediterranean rainfall anomalies are associated with large-scale, high-amplitude NA climate variability. Manifested over Greenland as persistent O(50 m) geopotential height anomalies, this variability perturbs the climatological configuration of planetary waves. Accompanying the Greenland anomalies is a second, reversed-polarity node over south-central Europe and the Mediterranean. Consequently, elevated Greenland pressure is consistent with an anomalous cyclone over the Mediterranean, while a Mediterranean high pressure system accompanies reduced pressure over Greenland. In the EM, such pressure anomalies result in anomalous meridional winds: southerlies during Greenland highs, and northerlies during Greenland lows. EM southerlies advect warm air into the EM, while northerlies cool locally. Because heat advection by horizontal and vertical motions dominate the thermodynamic equation of the EM (Rodwell and Hoskins 1996), cooling by horizontal winds is dynamically consistent with enhanced subsidence. Conversely, warming by anomalous EM southerlies is linked to enhanced ascent. Figure 11 makes the link between vertical and horizontal advection anomalies, and between them and the rain anomalies, more explicit. The figure shows that EM winter isentropes (the labeled contours) slope down toward the south at all times. Consequently, isentrope-following near-adiabatic meridional winds (section 3c) subside when flowing north to south during periods of reduced rainfall (Fig. 11a) and ascend when flowing south to north during periods of enhanced rainfall (Fig. 11b). Because the principal variability of water vapor is its rapid decrease with height, the vertical motions profoundly affect the moisture budget of the lower troposphere. During northward up-gliding (Fig. 11b) the lower troposphere is downstream of the moist boundary layer, and is thus being advectively moistened. Conversely, subsidence (Fig. 11a) dries the lower troposphere by advecting into it dry air from aloft. By modifying large-scale condensation and static stability with respect to moist ascent, these moisture advection patterns directly affect the intensity of deep convection and rain generation, causing the observed EM rainfall anomalies this paper wishes to explain.

Acknowledgments. GE thankfully acknowledges the generous hospitality of the Department of Earth and Planetary Sciences at Harvard and the Department of Physical Oceanography at the Woods Hole Oceano-

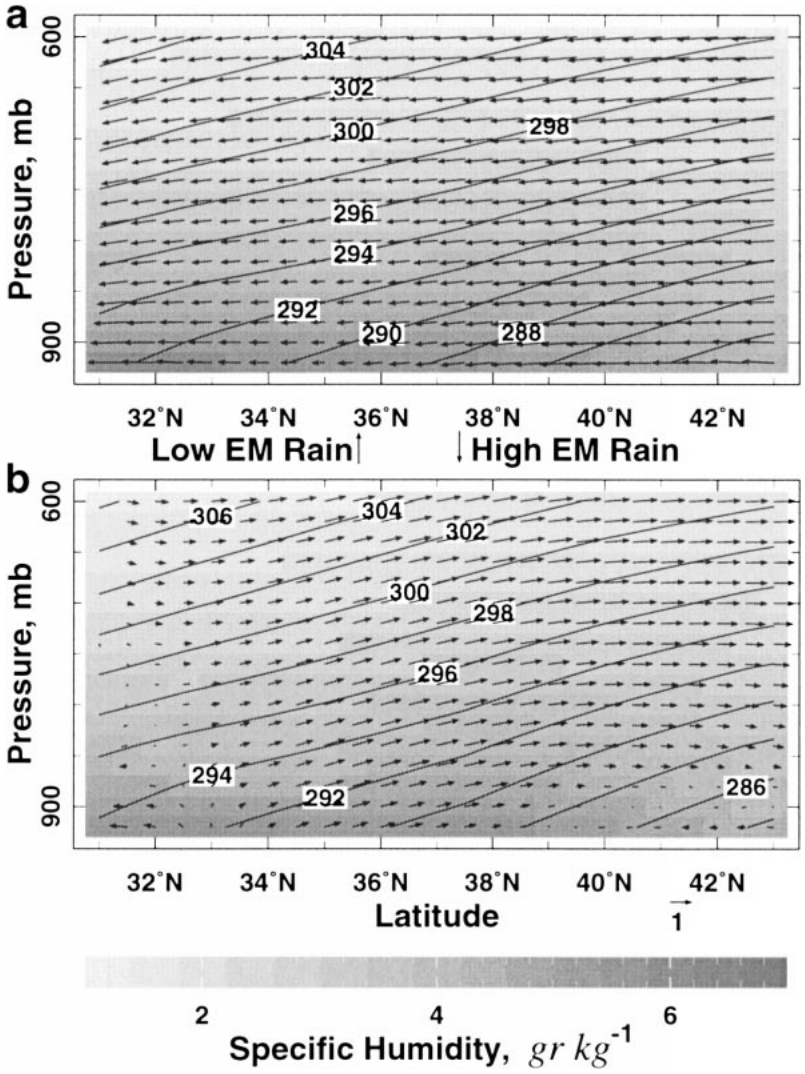

FIG. 11. Height–latitude sections averaged over 28°–34°E during EM rain extremes of total fields (i.e., not anomalies). Grayscale shading indicates specific humidity in g kg^{-1}; contours present θ_v (virtual potential temperature, K); and the vectors are of $[v \quad -10\omega]$, where v is the meridional velocity in m s^{-1} and ω is dp/dt in Pa s^{-1} [a scale arrow is displayed near the lower-left corner of (b)].

graphic Institution, and the support of the UCAR–NOAA Climate and Global Change Fellowship. BF was supported by NSF ATM-96132362. We thank two anonymous reviewers for their thoughtful comments, and Benno Blumenthal of the IRI at Lamont for creating Ingrid, the finest climate data archive and analysis language one can imagine.

REFERENCES

Baker, C. B., J. K. Eischeid, T. R. Karl, and H. F. Diaz, 1995: The quality control of long-term climatological data using objective data analysis. Preprints, *Ninth Conf. on Applied Climatology*, Dallas, TX, Amer. Meteor. Soc., 150–155.

Battisti, D. S., U. S. Bhatt, and M. A. Alexander, 1995: A modeling study of the interannual variability in the North Atlantic Ocean. *J. Climate,* **8,** 3067–3083.

Bladé, I., 1997: The influence of midlatitude ocean–atmosphere coupling on the low-frequency variability of a GCM. Part I: No tropical SST forcing. *J. Climate,* **10,** 2087–2106.

daSilva, A., A. C. Young, and S. Levitus, 1994: *Algorithms and Procedures.* Vol. 1, *Atlas of Surface Marine Data 1994, NOAA Atlas NESDIS 6*.

Frankignoul, C., 1985: Sea surface temperature anomalies, planetary waves, and air–sea feedback in the middle latitudes. *Rev. Geophys.,* **23** (4), 357–390.

Holton, J. R., 1992: *An Introduction to Dynamic Meteorology.* 3d ed. International Geophysics Series, Vol. 48, Academic Press, 511 pp.

Hulme, M., 1992: A 1951–80 global land precipitation climatology for the evaluation of General Circulation Models. *Climate Dyn.,* **7,** 57–72.

——, 1994: Validation of large-scale precipitation fields in General Circulation Models. *Global Precipitation and Climate Change*, M. Desbois and F. Desalmand, Eds., NATO ASI Series, Vol. I26, Springer-Verlag, 387–405.

Hurrell, J. W., 1995: Decadal trends in the North Atlantic oscillation: Regional temperatures and precipitation. *Science,* **269,** 676–679.
——, and H. van Loon, 1997: Decadal variations in climate associated with the North Atlantic oscillation. *Climatic Change,* **36,** 301–326.
Kalnay, E., and Coauthors, 1996: The NCEP/NCAR 40-Year Reanalysis Project. *Bull. Amer. Meteor. Soc.,* **77,** 437–471.
Kushnir, Y., 1994: Interdecadal variations in North Atlantic sea surface temperature and associated atmospheric conditions. *J. Climate,* **7,** 141–157.
——, 1999: Europe's winter prospects. *Nature,* **398,** 289–291.
——, and J. M. Wallace, 1989: Low-frequency variability in the Northern Hemisphere winter: Geographical distribution, structure and timescale dependence. *J. Atmos. Sci.,* **46,** 3122–3142.
Latif, M., and T. P. Barnett, 1994: Causes of decadal variability over the North Pacific and North America. *Science,* **266,** 634–637.
——, and ——, 1996: Decadal variability over the North Pacific and North America: Dynamics and predictability. *J. Climate,* **9,** 2407–2423.
McCartney, M. S., 1997: Is the ocean at the helm? *Nature,* **388,** 521–522.
Molteni, F., and T. N. Palmer, 1993: Predictability and finite-time instability of the northern winter circulation. *Quart. J. Roy. Meteor. Soc.,* **119,** 269–298.
Philips, J. L., 1982: *How to Think about Statistics.* Freeman and Company Press, 198 pp.
Rodwell, M. J., and B. J. Hoskins, 1996: Monsoons and the dynamics of deserts. *Quart. J. Roy. Meteor. Soc.,* **122B,** 1385–1404.
——, D. P. Rowell, and C. K. Folland, 1999: Oceanic forcing of the wintertime North Atlantic Oscillation and European climate. *Nature,* **398,** 320–323.
Steinberger, E. H., and N. Gazit-Yaari, 1996: Recent changes in the spatial distribution of annual precipitation in Israel. *J. Climate,* **9,** 3328–3336.
Trenberth, K. E., and C. J. Guillemot, 1998: Evaluation of the atmospheric moisture and hydrological cycle in the NCEP/NCAR reanalyses. *Climate Dyn.,* **14,** 213–231.
Venzke, S., M. R. Allen, R. T. Sutton, and D. P. Rowell, 1998: The atmospheric response over the North Atlantic to decadal changes in sea surface temperature. Max-Planck-Institut für Meteorologie Rep. 255, 46 pp. [Available from Max-Planck-Institut für Meteorologie, Bundesstrasse 55, D-20146 Hamburg, F.R. Germany.]
Wallace, J. M., C. Smith, and Q. Jiang, 1990: Spatial patterns of atmosphere–ocean interactions in the northern winter. *J. Climate,* **3,** 990–998.
——, ——, and C. S. Bretherton, 1992: Singular value decomposition of wintertime sea surface temperature and 500-mb height anomalies. *J. Climate,* **5,** 561–576.
Weng, W., and J. D. Neelin, 1998: On the role of ocean–atmosphere interaction in the midlatitude interdecadal variability. *Geophys. Res. Lett.,* **25** (2), 167–170.